# Dielectric Metasurface Inspired Directional Multi-Port Luneburg Lens as a Medium for 5G Wireless Power Transfer—A Design Methodology

Basudev Majumder, *Member, IEEE*, Sarath Sankar Vinnakota, Siddharth Upadhyay, and Krishnamoorthy Kandasamy

***Abstract*—In this paper, a novel dielectric metasurface-inspired multi-beam directional Luneburg lens is proposed as a wireless power transfer medium at 5G mm-wave band. The lens is constructed using dielectric-based unit cells made up of a glide symmetric approach. It is connected with a set of microwave detector integrated multi-port tapered rectangular feeds to convert the received RF energy from different directions to DC power across a combined load. The proposed structure can be a potential candidate to harvest ambient energy from a wide coverage range of around 160° and produce a power conversion efficiency of about 76% for an input power of 14.9 dBm at 24 GHz.**

***Index Terms*—Glide symmetry, engineered periodic structures, luneburg lens, sensing, wireless power transfer.**

## I. Introduction

IN THE present world, when millions of devices are connected with Internet of things Technology (IoT) technology [1], it has become a challenge to power them from constant and reliable sources. Powering the sensors can be made possible through solar [2], thermal [3] and other energy harvesting technologies [4]. Due to certain disadvantages associated with these technologies, in the recent past, wireless power transfer (WPT) technique came up as one of the promising technology for battery-less charging. There are majorly three wireless powering techniques possible. They are magnetically coupled coils using magnetic resonance, near field induction mode, and far field wireless powering techniques. The third technique deals with harvesting low power ambient energy with an antenna and rectifier topology, which together are generally termed as rectenna [5].

The main challenge of WPT technology is that the ambient RF power density is very low, and the harvested DC voltage does not become sufficient to drive the low-power IoT-connected sensors. Many techniques have been employed and reported in the literature to overcome this. One such technique which can be found very common in the literature is to improve the power conversion efficiency (PCE) using multi-band rectennas [6], [7], dual-band antennas [8], [9], triple-band antennas [10], quad-band antennas, and hexa-band rectennas [11] have been proposed. Broadband rectennas are also investigated [12], [13] as a potential candidate for WPT. Recently, multi-port rectennas with spatial [14], angular [15] and polarization [16], [17] are widely studied and its power conversion efficiencies are also reported.

With the advent of the 5G technology, the base station for 5G has unknowingly become a reliable source and can act as a useful wireless power grid. On the other hand, in the mm-wave 5G band (>24 GHz), the allowable effective isotropic radiated power (EIRP) has been pushed beyond 75 dBm at a distance of 100 meters away from the transmitter by the Federal Communication Commissions (FCC) as compared to the 3 G and 4 G frequency bands. This opens up the opportunity of powering the devices with a wide range of distances. The opportunities and the related key challenges for the systems in the 5G frequency band and above are elaborated in the work [18]. In the 5G mm-wave band (at 24 GHz), minimal effort has been made to study the performance of the rectennas. In the works [19]–[23] some attempts have been made to study their performance, like in [20] a rectenna is described with 54 % efficiency, driven by 130 mW of input power and 41 % of efficiency with 50 mW power.The development of CMOS-based rectenna [24], [25] has also become popular due to its ever-decreasing cost. A CMOS-based rectenna is reported in [24] where 37% of PCE is reported at 35GHz. So, the obtained PCE in the mm-wave range is still low. In [26] authors have analytically and experimentally verified through an RF energy harvesting experiment that the average output DC power is non-linearly dependent on the directivity of the antenna but linearly dependent on the number of ports. In the 5G band, directive phased array antennas and switched beam antennas with conventional feed networks do not seem feasible due to their high radiating loss.

Harvesting power from a wide range of angular directions is highly desirable since the relative orientations of the source, and the harvesters are generally unknown. Recently, the work [27] proposed omnidirectional rectenna array using the vivaldi

Manuscript received April 1, 2022; accepted April 18, 2022. Date of publication April 25, 2022; date of current version May 4, 2022. This work was supported by the DST Inspire Faculty Award under Grant IFA17-ENG197. *(Corresponding author: Basudev Majumder.)*

Basudev Majumder and Siddharth Upadhyay are with the Microwave Electronics Division, Department of Avionics, IIST, Thiruvananthapuram, Kerala 695547, India (e-mail: bmbasudev30@gmail.com; saddhart10@gmail.com).

Sarath Sankar Vinnakota is with the Department of Electrical and Electronics Engineering, BITS-Pilani, Hyderabad Campus, Telangana 500078, India (e-mail: sarath.vinnakota@gmail.com).

Krishnamoorthy Kandasamy is with the Department of Electronics and Communication Engineering, NITK-Surathkal, Karnataka 575025, India (e-mail: krishnak_ece@yahoo.com).

Digital Object Identifier 10.1109/JPHOT.2022.3169711

antennas with multi-frequency coverages in the lower frequency bands of 1.7–1.8 GHz and 2.1–2.7 GHz for IoT applications. In [28], a Rotman lens-based series fed patch antenna array is proposed to harvest energy from 5G band and analyzes the trade-off between the angular coverage and the turn-on sensitivity of the rectifier. The lens has a limited coverage (110°) within its narrow band, although it provides multiple beams. To harvest energy from the 5G band, multi-port directional and low profile 2D lens antennas can become a very potential candidate due to their wide scanning range and compact footprint as compared to their 3D counterpart. Among various types of lenses, Luneburg lenses are very popular to microwave and optical engineers [29]–[35]. In this type of lens, the material is spatially varied to form a gradient refractive index (GRIN) surface. In the works [36]–[39] different suitably designed 2D periodic metasurfaces have been explored for designing Luneberg lenses. Like in [37]–[40] different glide symmetric based metallic and dielectric unit cells are periodically arranged along the X and Y direction to achieve the GRIN profile. The authors in [41] investigate a two-dimensional glide-symmetric periodic dielectric unit cell and show that as compared to non-glide arrangements, glide symmetry removes the limitation of the narrow bandwidth and results in broadening the operating bandwidth and in lowering effective refractive indices with increased isotropy. In the recent past, authors in [42] have used rectifier integrated metallic Luneburg lens for wireless power transfer in 5G mm-wave band. However, it does not cover a wide and continuous coverage range, and also the DC combining does not produce good PCE over a fixed RF power density.

As a result, the need for an mm-wave rectenna operating at 5G frequency having a wide coverage range and high power conversion efficiency for a fixed available input RF power density has motivated our research. First, the modal behaviour of a dielectric material-based glide symmetric unit cell is characterized over a wide range of frequency bands. Then this unit cell is arranged to form the Luneburg surface for converting the received directional planar wave-front into its focus. Subsequently, a set of rectangular tapered waveguide feed and an optimized flare is designed to receive the power from a broad and continuous coverage range and to match the lens aperture impedance to the free space impedance. Next, an inverse class F based [43] shunt topology made up of a suitable rectifying diode [19] with the optimized matching circuit is integrated with the previously designed waveguide feed. The rectification currents from all the ports have been combined and delivered to a common load for better efficiency enhancement. The entire system is designed and numerically verified in a step-by-step manner. Unlike [27] the proposed rectenna system focuses at high frequency to exploit the advantage of high EIRP at 5G mm wave band and investigates its overall efficiency under a common driving load (or sensor nodes) for constant and regulated voltage using the shunt topology. Also the proposed structure uses Luneburg surface as beam-former-cum-antenna thereby reducing the need for using separate radiators like in [28] and also can provide wide field field of view.

The paper is organized as follows, Section II deals with analyzing the unit cell behavior and the synthesizing the lens aperture. This particular section also describes the necessary design equations, simulation results and the performance of the constructed lens. Section III explains the design of suitable rectifier topology and Section IV reports the seamless integration of the rectifier with the lens for the rectification performance enhancement. Finally, a conclusion of the presented work is drawn in Section V.

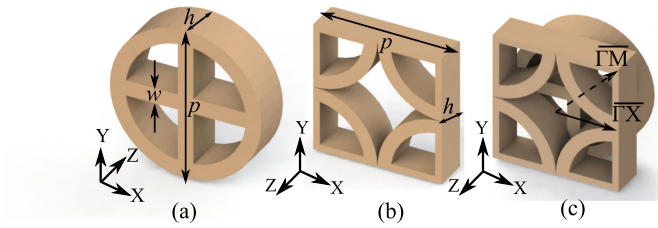


Fig. 1. Unit cell Construction (periodicity $p = 3.7$ mm and height $h = 1$ mm) (a) Bottom Layer (b) Top Layer (c) Overall unit cell.

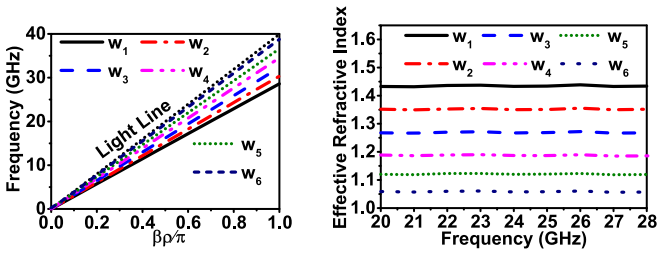


Fig. 2. (a) Mode 1 curves for various unit cell dimensions used in lens (b) Refractive index variation with frequency $w_1 = 1$, $w_2 = 0.58$, $w_3 = 0.38$, $w_4 = 0.23$, $w_5 = 0.13$, $w_6 = 0.05$ (dimensions in mm)

## II. Design and Analysis of the Multibeam Lens

### A. Unit Cell Design and Analysis

The unit cell structure is shown in Fig 1. The top and bottom layers are represented in Fig. 1(a) and (b) respectively. The top layer is constructed by applying glide symmetry on the bottom layer of the unit cell $((x, y, z) \rightarrow (x + p/2, y + p/2, -z))$, where $p$ is the periodicity of the unit cell. The complete unit cell design is shown in Fig. 1(c). The dielectric material used to construct this unit cell is having a permittivity of 2.33 and a loss tangent of 0.0012. The proposed structure is arranged periodically along the X and Y directions in a parallel-plate waveguide configuration (i.e., with perfect electric boundary at the top and bottom of the structure along the Z-direction). Fig. 2(a) shows the variation of the first mode with the unit cell width ($w$). It is calculated using the Eigenmode solver of the commercially available electromagnetic simulation tool CST MWS. The higher linearity of the mode 1 curve signifies that the equivalent refractive index will remain invariant over the wide bandwidth. The equivalent refractive index reported in Fig. 2(b) has been extracted from these modes. To obtain the necessary refractive index, the width ($w$) of the unit cell is modulated between 0.05 mm and 1 mm, and it is observed that

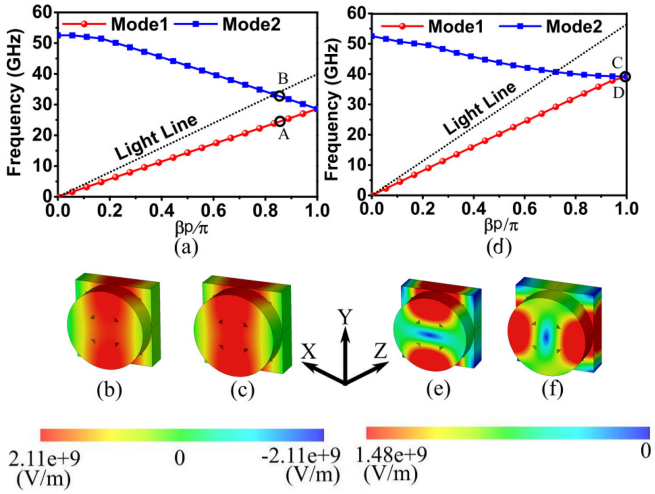


Fig. 3. For $\overline{\Gamma X}$ (a) Dispersion diagram; Electric field component ($E_z$) (b) Mode 1 (Point A) (c) Mode 2 (Point B); For $\overline{\Gamma M}$ (d) Dispersion diagram; Electric field ($E_z$) Component (e) Mode 1 (Point C) (f) Mode 2 (Point D).

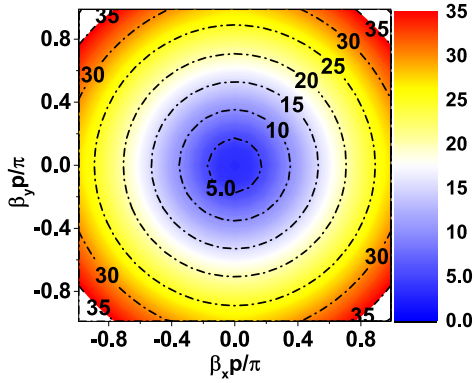


Fig. 4. Isofrequency curves for lowest order mode.

the refractive index reduces with the decrease in width ($w$). It is also seen that the height of the proposed unit cell has minimal impact on the refractive index variation. The Fig. 3 reports the first two modal behavior of the proposed glide symmetric unit cell along the propagation direction X ($\overline{\Gamma X}$) and along the diagonal ($\overline{\Gamma M}$). The proposed unit cell being geometrically and electrically symmetric and isotropic in nature along both the X and Y directions, characterization along the Y direction is not reported. In order to understand the modal behavior of the lowest order two modes along both the direction (as mentioned in Fig. 3(a) and (d)), the electric field component along Z-direction, $E_z$, (for $\overline{\Gamma X}$ direction, and for $\overline{\Gamma M}$ direction, are reported. The two lowest order modes along the X direction are the branches of the same mode. The similar modal field distributions reported in Fig. 3(b) and 3(c) (of point A and B, respectively in Fig. 3(a)) confirm the perfect correlation between these two modes. On the other hand, for $\overline{\Gamma M}$ direction the electric field component along Z-direction, $E_z$ at modal solutions point C and D, confirm that these two modes have zero modal correlation even though they appear to branch from a single point. The lowest order mode becomes the real propagative and the next higher order mode (mode 2) becomes evanescent in this case. This type of accidental degeneracy in two different modes can be observed from the presence of the Dirac points reported in 2D photonic crystals [44]. The electric field behaviour of the modal solutions explained above are in complete correspondence with the results computed by the application of the "Correlation Method" [45], [46]. The complete wave propagation of the proposed unit cell over a wide band of frequencies is studied in the isofrequency curve for mode 1 and shown in Fig. 4. It can be seen that, due to the circular shape of the dispersive modal solutions, the phase velocities along both the X and Y directions, remain uniform between 5 GHz up-to 35 GHz. However, this isotropic behaviour at very high frequency (more than 40 GHz) tend to degrade and the unit cell becomes more anisotropic in nature. Next, the proposed unit cell is characterized using the frequency domain analysis method with suitable boundary conditions in parallel plate environments in order to gain a deeper physical insight on the relevant consequence of the constitutive parameters. In all of these analysis unless specified, period ($p$) of the unit cell is 3.7 mm and the height is 2 mm. Since the thickness of the unit cell along the direction of the propagation is smaller as compared to its operating wavelength, its electromagnetic properties can be extracted using the effective medium theory (EMT) approach. The extraction of the permittivity and permeability starts with the reduction of values of effective refractive index $n_{eff}$ and effective wave impedance $Z_{eff}$ whose values can be obtained directly from its scattering responses. The following equations give the relationship among these parameters [47].

$$Z_{eff} = \pm\sqrt{\frac{(1+S_{11})^2 - S_{21}^2}{(1-S_{11})^2 - S_{21}^2}} \tag{1}$$

$$\eta_{eff} = \frac{-i}{k_0 p} ln\left(\frac{S_{11}}{1 - S_{21}\left(\frac{z_{eff}-1}{z_{eff}+1}\right)}\right) \tag{2}$$

$$n_{eff} = \sqrt{\mu_{eff}\epsilon_{eff}} \tag{3}$$

where $S_{11}$ and $S_{22}$ correspond to the magnitudes of reflection and transmission coefficients, and $k_0$ is the propagation constant. While calculating the above parameters using the Multi-mode Bloch technique [48], [49], suitable number of higher order modal fields have been considered in order to have a good reconstruction of the scattering responses and to get an insight of the global propagation and attenuation constant [50]. The dimension of the unit cell used for this analysis is kept the same as that of the eigen-mode analysis. From Fig. 5(a), it can be seen that the extracted refractive index ($\eta_{eff}$) plot calculated from the scattering responses of it matches with the one which is obtained from the eigen-mode analysis. The extracted permittivity ($\epsilon_{eff}$) values for different width is shown in Fig. 5(b). From this figure, it can be observed that the permittivity tends to decrease as width ($w$) decreases and has a minimal variation with the frequencies. Figs. 6 and 7 depict the efficacy of the glide symmetric structure over the non-glide one in constructing a wide-band lens. Fig. 6 represents two lowest order modes for both glide and non-glide symmetric structure (for $w = 1$ mm) calculated using eigen

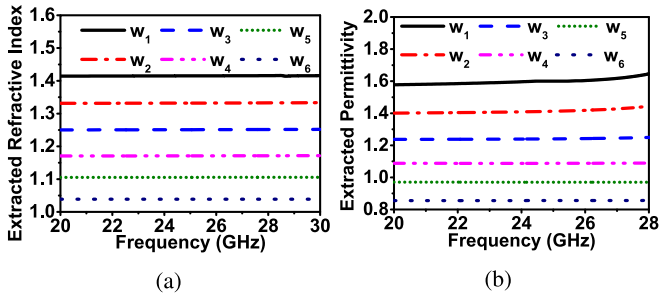


Fig. 5. (Refer Fig. 2 for dimensions of '$w$') (a) Extracted refractive index variation over frequency (b) Permittivity variation over frequency

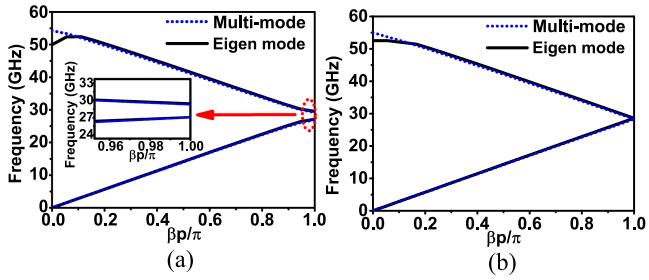


Fig. 6. Comparison of multi-mode Bloch analysis and eigen mode analysis $\overline{\Gamma X}$ ($w = 1$ mm) (a) Non-glide unit cell (b) Glide symmetric unit cell.

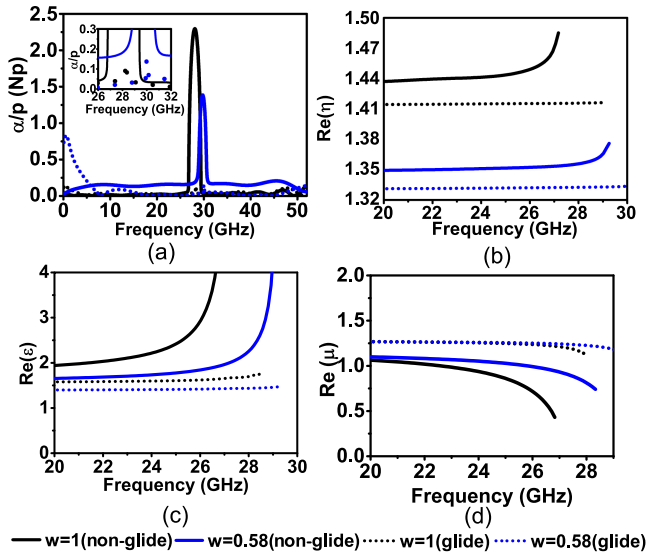


Fig. 7. For glide-symmetric (Fig. 1(c) $p = 3.7$ mm and $h = 2$ mm) and non-glide-symmetric (Fig. 1(a) $p = 3.7$ mm and $h = 2$ mm) unit cells (a) Comparison of attenuation loss (b) Real part of RI (c) Real part of the permittivity (b) Real part of the permeability.

mode as well Multi-mode Bloch analysis. Non-glide symmetric structure exhibits a strong band-gap as can be seen from the inset of Fig. 6(a), whereas the glide symmetric structure does not show any bandwidth limitation and its frequency of the lowest order mode extends till 55 GHz which is also previously verified by its modal E-field distribution ($E_z$) in Fig. 3. The elimination of the band-gap zone results in more linear modal behaviour of the lowest order mode and thereby a uniform refractive index over the wide band of frequencies. This fact has been further verified in Fig. 7(a) with the extracted attenuation constant value ($\alpha$) per period for an unit cell of $w = 1$ and $w = 0.58$ mm. It shows that the non-glide symmetric unit cells have almost zero attenuation per period. These facts are highly required for designing wide band lenses. Fig. 7(b) represents the extracted refractive index ($\eta$) variation for a 'X' directed propagating wave for both non-glide symmetric (solid curve) and glide symmetric (dotted curve) structures. It can be seen from these curves that for the same period value the one with lower width (blue color) is less disturbed by the corrugation as compared to that of the one with higher width (black color) and results in lower value of the extracted refractive index. Also, the bandwidth of the non-glide symmetric case is observed limited as previously described. Fig. 7(c) and 7(d) report the constitutive parameters of the glide (dotted) and the non-glide (solid) symmetric unit cell structure. The similar nature can also be seen from the extracted permittivity values reported in the Fig. 7(c). Fig. 7(d) shows the extracted permeability ($\mu$) along X directing propagating plane wave. The extracted permeability of the glide symmetric structure is observed more than its non-glide counter part. This fact indicates that the glide structure exhibits strong magnetic behaviour. The variation of the extracted refractive index illustrated in Fig. 7(b) is majorly due to the variation of both these constitutive parameters. The unit cell structure being isotropic in nature the characterization for the propagating wave along the Y direction is not reported. These above mentioned comparative investigations brings about the efficacy and the advantage of having the glide symmetric unit cell over non-glide counter part.

### *B. Luneburg Lens Design and Analysis*

This subsection deals with designing a Luneburg lens with the unit cells already characterized in the previous subsection. The refractive index variation of the Luneburg lens is given by the equation [39]

$$\eta_{eff} = \sqrt{2 - (r/R)^2} \tag{4}$$

where $R$ is the radius of the unit cell and $r$ is the variable distance from the origin to the periphery of the lens. The lens design includes a unit cell of six different refractive indices, which are arranged in six different layers circularly. The unit cell ($w = 1$ mm) having a refractive index of 1.43 is arranged at the center of the lens. The unit cell ($w = 0.05$ mm) of refractive index 1.06 is arranged at the periphery with the radial distances ($r$) calculated based on (4). The variation of the refractive indices with the unit cell width is shown in Fig. 8(a), and this variation can be represented using the equation (5) and is not dependent on frequency.

$$\eta_{eff} = 1.0248 + 0.78093w - 0.36673w^2 \tag{5}$$

The arrangement of unit cell is shown in Fig. 8(b). The Fig. 9 gives the design construction phases of the overall final lens. The Fig. 9(c) shows the effective refractive index distribution for a single quadrant of the lens as calculated by (4). As illustrated in Fig. 9, the complete lens is built using this design to cover all four quadrants. Fig. 9(b) shows one such quadrant. A flare

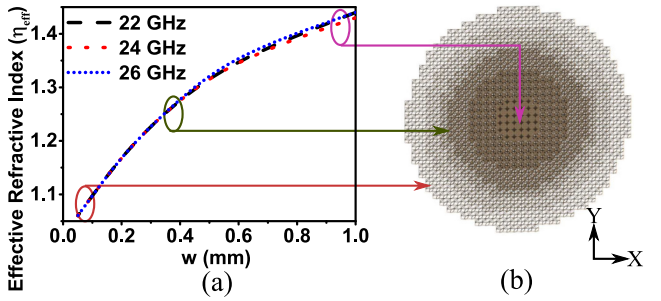


Fig. 8. (a) Refractive index variation with width (b) Metasurface lens showing corresponding parts.

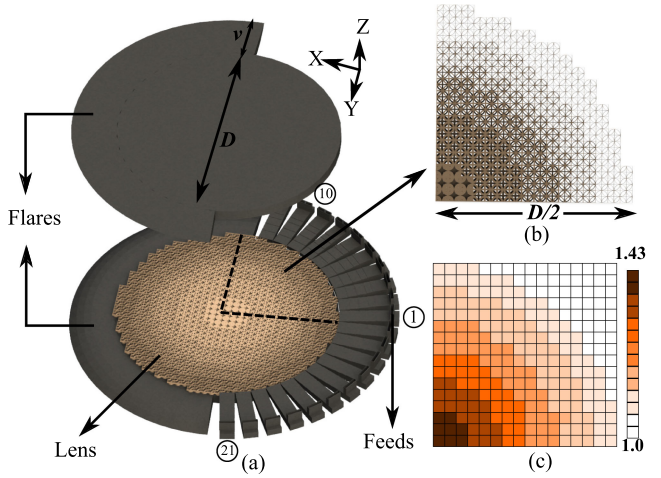


Fig. 9. Lens construction (a) Exploded view: $D = 118$ mm, $v = 24$ mm (b) Quadrant of the lens (c) Luneburg RI profile for single quadrant.

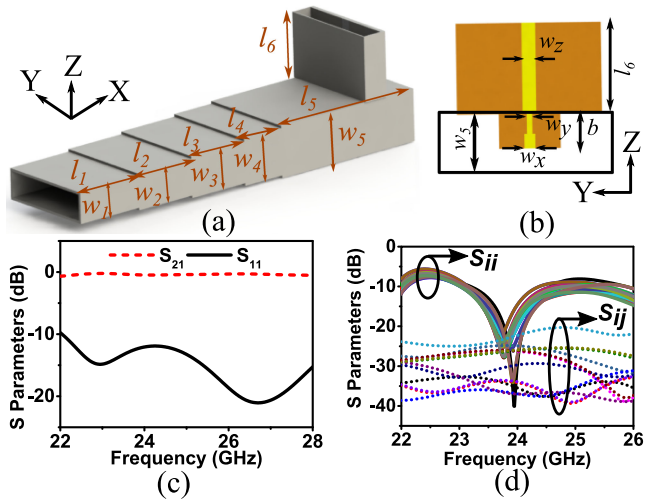


Fig. 10. (a) Dimensions of the waveguide to microstrip transition (in mm) $l_1 = 5.5, l_2 = 5, l_3 = 5, l_4 = 3.5, l_5 = 12.5, l_6 = 5, w_1 = 2.4, w_2 = 2.8, w_3 = 3.2, w_4 = 3.6, w_5 = 4$ (b) Optimized dimensions of the probe (in mm): $w_x = 0.6, w_y = 0.3, w_z = 0.76, b = 1.9$ (c) Scattering response of the transition (d) Scattering response of the lens with the transition (reflection coefficients ($S_{ii}$) and cross talk ($S_{ij}$), $i$ and $j$ represent port indices).

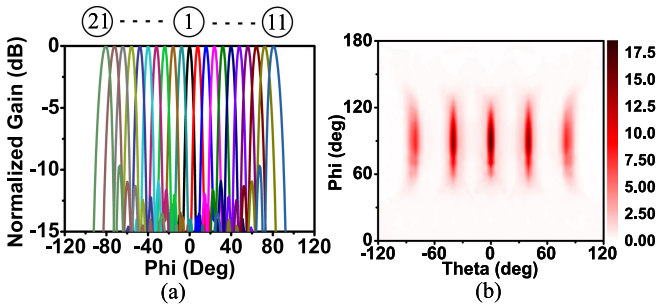


Fig. 11. (a) Normalized Radiation Patterns for the ports at 24 GHz (b) 2D radiation plot at 24 GHz (Only fewer plots shown for clarity).

structure similar to that in [42] is added to match the lens aperture impedance to the free space. The lens diameter is chosen at 118 mm to ensure that the antenna delivers the acceptable beam-width for WPT applications [42]. Using this design methodology, the exploded view of complete lens structure is shown in Fig. 9(a).

The Fig. 10 depicts the feeding network configuration where the present system is driven by a waveguide to microstrip transition [51], that employs a conventional and compact WR28 waveguide. The feed waveguide section of the structure is optimized in this proposed work by incorporating E-plane step transitions to operate in the desired frequency range. The microstrip transition is comprised of an E-field probe that is set to cancel the imaginary portion of the input impedance, allowing for maximal electric field coupling between the waveguide (with $TE_{10}$ mode) and the microstrip line (with quasi TEM mode). The probe is located around a distance of $\lambda/4$ from the back-short of the waveguide to couple the E-field efficiently and yield better impedance matching. The whole structure is built on an RT Duroid 5870 substrate with a 0.254 mm thickness. The optimized dimensions of the waveguide, the E-field probe, and the transition are depicted in Fig. 10. The optimized E-field probe is inserted into the waveguide and is represented in Fig. 10(b). In addition, the scattering responses of the transition are also shown. Fig. 10(c) shows that the transition is appropriate for use in the intended frequency range. This waveguide to microstrip transition has the benefit of allowing the structure to span a larger and more continuous scanning range. The feeding structure is then fed into the radiating lens design, which is subsequently stimulated via a discrete port. Twenty one such feeds are symmetrically positioned (10 on each side, as shown in Fig. 9(a)) along the main feed to increase the lens coverage. The angle between any two successive feeds is 8°, and the design is simulated using CST 2019 in a High Performance Computing (HPC) environment. Fig. 10(d) shows the reflection coefficient of the overall lens along with the cross talk. It can be seen that all the 21 ports have a desirable reflection coefficient response ($S_{ii}$) less than $-15$ dB with minimum reflection at 24 GHz and the cross-talk between any two ports ($S_{ij}$) in Fig. 10(d)) is observed to be less than $-19$ dB.

The normalized radiation pattern at 24 GHz for all 21 ports is shown in Fig. 11(a) verifying that the lens covers a wide scanning range of $-80°$ to 80°. The 2D radiation patterns for

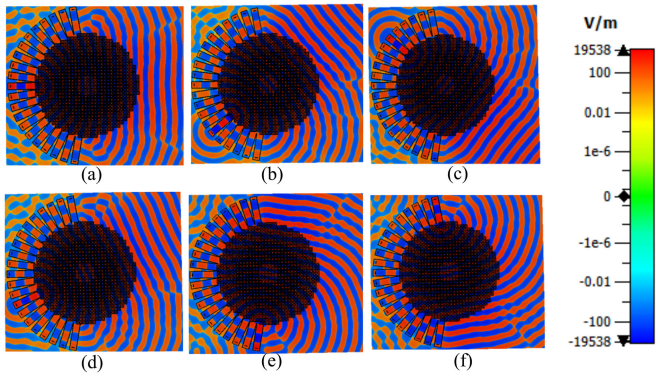


Fig. 12. Electric field distribution at 24 GHz (a) Port 1 (b) Port 6 (c) Port 16 (d) Port 4 (e) Port 11 (f) Port 21.

TABLE I
COMPARISON OF PROPOSED STRUCTURE WITH SIMILAR LUNEBURG LENSES DESIGNED AT VARIOUS FREQUENCIES

| Ref. | Lens Type | Lens Dia | Freq /GHz | Rad. Eff. % | Gain[@] /dBi | Scan Angle |
|---|---|---|---|---|---|---|
| **PW*** | **3D printing low cost** | **9.4$\lambda_0$** | **24** | **85** | **19.6** | **$\pm 80^0$** |
| [42] | Metallic parallel plates | 9.4$\lambda_0$ | 24 | 87 | 17.2 | $\pm 36^0$ |
| [28] | PCB | 7.11$\lambda_0$ | 28 | NA | 17 | $\pm 55^0$ |
| [52] | 3D Printing | 4.2$\lambda_0$ | 26.75 | 50 | 12 | NA |
| [41] | 3D Printing | 4.66$\lambda_0$ | 28 | 70 | 19.4 | $\pm 50^0$ |
| [53] | Plastic-filled metal parallel plates | 4.8$\lambda_0$ | 29 | NA | 12 | $\pm 50^0$ |
| [54] | Air-filled metal parallel plates | 13.8$\lambda_0$ | 30 | 71 | 16.6 | $\pm 80^0$ |
| [55] | PCB - stacked | 13.7$\lambda_0$ | 31.5 | 35 | 96 | $\pm 72^0$ |
| [56] | Metallic parallel plates | 4.4$\lambda_0$ | 33 | 87.8 | 16.5 | $<\pm 50^0$ |
| [57] | Printed Substrate with drilled holes | 6.5$\lambda_0$ | 79.5 | 63 | 12.3 | $<\pm 50^0$ |

*PW: Proposed Work (Simulated), [@]Peak Gain, $\lambda_0$: center frequency, Rad. Eff.: Maximum radiation efficiency

five different ports at equal intervals are plotted to compare the variation of radiation intensity of the symmetric ports to that of the central port. As seen in Fig. 11(b), the patterns confirm that the radiation intensity slightly reduces when we move from the central port to the periphery of the lens. The realized gain of the two extreme ports of the lens are found to be 16.1 dBi which is 3 dB down from the central port. The gains of the other ports are observed to vary between 16.1 dBi and 19.6 dBi (from 23 to 26 GHz), depending upon their proximity to the central feeding. The Luneburg lens converts the spherical wavefront generated from the radiation feed at one end of the lens to a planar wavefront at the diametrically opposite end, leading to an increase in the directivity. This phenomenon is further verified by its simulated e-field ($E_z$) distribution in Fig. 12. The radiation efficiency of the lens is found to be greater than 80% over the bandwidth. Finally, the performance of the proposed Luneburg lens is compared to the other proposed lens structures reported in the literature at different frequencies as indicated in Table I. It can be concluded that the lens occupies a smaller size (lens diameter of 9.4$\lambda_0$), provides a higher peak gain (19.6 dBi), and a wider scanning angle (from $-80°$ to $80°$) compared to the other reported Luneburg lenses.

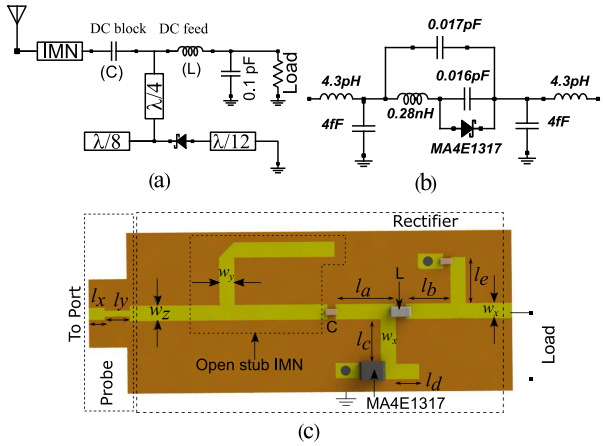


Fig. 13. (a) Schematic of the inverse class F rectifier (b) MA4E1317 Diode model with parasitics [61], [62] (b) Layout realization of the rectifier (Dimensions in mm): $l_x = 0.8$, $l_y = 1.25$, $l_a = 1$, $l_b = 1$, $l_c = 2.3$, $l_d = 1.14$, $l_e = 2.3$, $w_x = 0.4$, $w_y = 0.3$, $w_z = 0.76$.

## III. RECTIFIER CIRCUIT DESIGN

Since the Luneburg lens converts the received planar wavefront from all the directions into its focus, where the feeds are located, it needs to be integrated with corresponding rectifying circuits to extract the RF power ($P_{RF}$) into a DC power ($P_{DC}$) suitable for driving low power wireless sensor nodes. The figure of merit used to measure the conversion is called the power conversion efficiency (PCE) given by

$$\eta_{PCE}(\%) = \frac{P_{DC}}{P_{RF}} * 100 \tag{6}$$

The rectifying circuit requires a non-linear device to accomplish this conversion. The article [58] proposes devices such as Schottky diodes, backward tunnel diodes, MIM diodes, spin diodes, out of which Schottky diodes have inherent advantages such as high responsivity and low-cost availability. These diodes can be realized into the rectifying circuit using several topologies such as series, shunt, voltage doubler, etc. Recently, class F topology has been proposed in [59], and it promises a better power conversion efficiency due to the presence of a harmonic termination network in its circuit. More recently, inverse class F topology is proposed in [60] and compared to the class F topology. Inverse class F topology showed a better performance in terms of peak power efficiency with reduced power losses. A variation of the inverse class F topology proposed in [43] is used to design the rectifier circuit in this proposed work. The circuit schematic of the inverse class F rectifier is shown in Fig. 13. The circuit consists of the Schottky diode MA4E1317 (including parasitic values taken from [61], [62]) with its anode connected to a grounded stub of length λ/12, and the cathode connected to an open stub parallel to a transmission line of length λ/8. This network is connected to the circuit consisting of the low pass filter and the impedance matching network. The capacitors are commercially available (KEMET) ultra-wideband variants with a capacitance of 0.1 pF. The substrate RT Duroid 5880 with 0.254 mm thickness is used for the rectifier design.

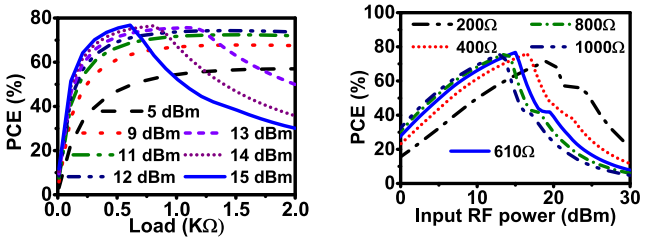


(a) (b)

Fig. 14. Variation of PCE with (a) load at various input power levels (b) input power at various values of load

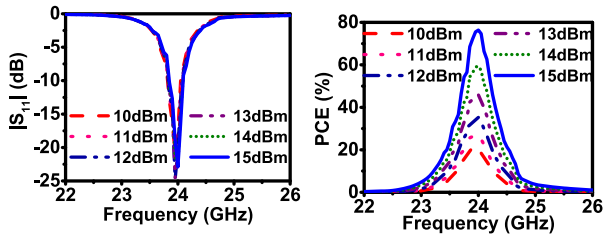


(a) (b)

Fig. 15. Variation of (a) reflection coefficient with frequency at various input power levels (b) PCE with frequency at various input power levels

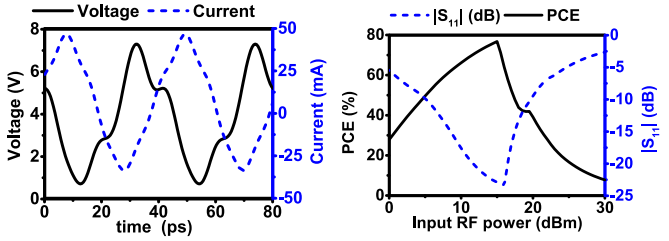


(a) (b)

Fig. 16. At 24 GHz (a) Inverse Class F voltage and current waveforms across the diode in circuit Fig. 13(b) (b) PCE and $S_{11}$ variation over input power for ideal inverse class F circuit shown in Fig. 13(a) and the designed circuit using microstrip lines shown in Fig. 13(b)

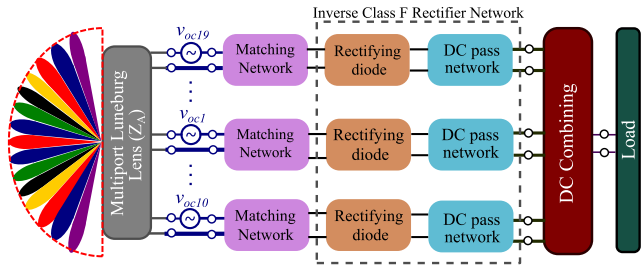


Fig. 17. Schematic of the overall proposed system.

In the first step of rectifier design, the inverse class F topology is realized without including the impedance matching network (IMN) to calculate the optimum load for the highest possible power conversion efficiency. To determine the optimal load, the load impedance is varied and its PCE is studied. As can be seen from the Fig. 14(a), for a fixed input power level, the peak efficiency is obtained at a particular load value and after this point the efficiency steadily drops. Also, for a fixed load value the efficiency increases with increased input power level till it reaches its maximum and the output load current saturates. Fig. 14(b) shows the PCE variation with input power level for different discrete loads. It can be concluded that for the higher load value, the maximum efficiency is obtained with less received input power level. The PCE for fixed load first increases for a particular input power level and then steadily drops. By investigating these figures, the correct optimal load value is selected to be 610 Ω at an input power level of 15 dBm.

This circuit is then matched to an impedance of 50 Ω. Fig. 15(a) presented here shows the variation of the reflection coefficient with frequency for different input power levels. It can be seen that even if the input power level varies between 10 dBm and 15 dBm the input matching is retained for a single rectification unit. Fig. 15(b) shows the PCE variation with frequency for the same input power levels. As can be seen from this figure, the input power changes the diode input impedance and hence the response of the matching circuit gets detuned which reflects into the degradation of efficiency. However, the overall efficiency remains between 20% and 76.5% over the input power level variation between 10 dBm and 15 dBm.

The results of the proposed design realized using microstrip lines are plotted in Fig. 16. The voltage and current waveforms of the inverse class F rectifier are plotted in Fig. 16(a). The circuit is optimized to find out the best possible load using the Harmonic Balance (HB) and Large Signal S-parameter (LSSP) blocks of the circuit simulation software Keysight ADS. It is observed from Fig. 16(b) that a maximum PCE of 76.5% is found for the optimum load of 610 Ω at an input power of 15 dBm.

## IV. Integration of the Rectifier With Luneburg Lens

The designed inverse class F rectifier is studied for wireless power transfer using a multiport Luneburg lens as a receiving structure and this design can harvest from a wide angular range. The concept of integrating all the ports of the lens into a wireless power transfer network, similar to the combining methods reported in [27], [42], [63], is illustrated in Fig. 17, where the power received by the lens is connected to the rectifying network using impedance matching networks. The term $v_{oc}$ denotes the open circuit voltages at the outputs of the individual ports. The current obtained from the end of each branch of port followed by the rectifying network are then combined and connected to a common load as shown in Fig. 17. Since each port of the lens has a different input reflection coefficient, the source impedance also varies as a consequence of it. Thus, the source impedance of each port is replaced with the corresponding impedance obtained from the Z-parameters of the proposed lens obtained from the simulation. All the mutual impedances of the ports have been taken into account to complete this study. Thus, 21 IMNs are designed to match the source impedances of the 21 ports to that of the rectifiers. The schematic of the lens integrated with individual rectifiers is illustrated in Fig. 18(a). As a final step, the power is combined by adding up the currents obtained

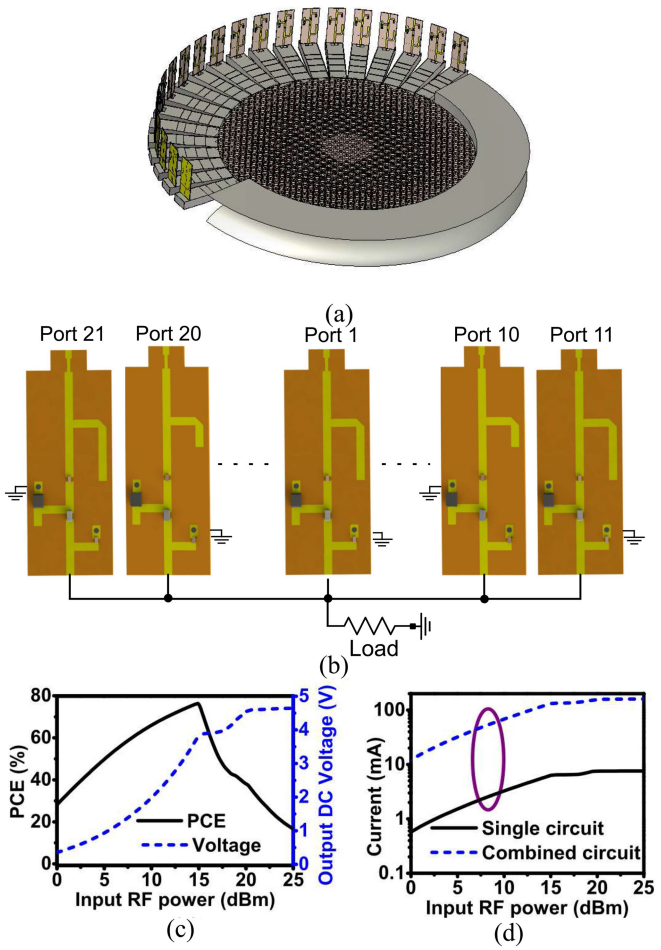


Fig. 18. (a) Rectifiers integrated to the Luneburg lens (top layer not shown) (b) DC combining network (c) Variation of output DC voltage and PCE with input RF Power at 24 GHz (d) Comparison of the load current with and without the DC combining network at 24 GHz.

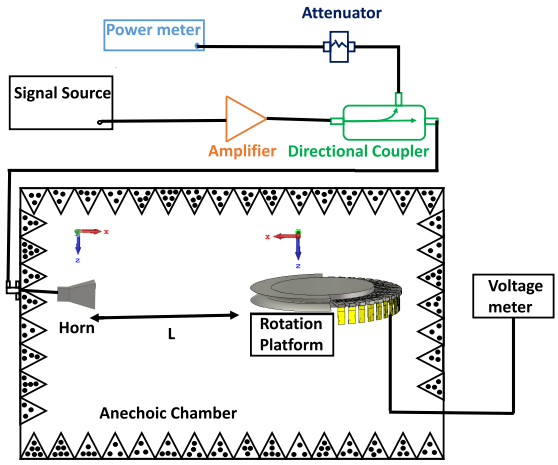


Fig. 19. Measurement setup in anechoic chamber.

from the individual rectifiers, (in other words, shunt rectenna topology [64]) and connecting all the outputs of the rectifiers to a common load, as shown in Fig. 18(b). This common load is calculated by dividing the optimum load with the number of rectifier circuits, in this case, 21, giving a value of 29 Ω.

The results obtained from this circuit are shown in Fig. 18(c) and (d). It can be inferred that the output DC voltage increases with the increasing input RF power. This increase in voltage continues until the diode reaches saturation due to the non-linear effects. The PCE obtained after combining the circuit is also plotted in Fig. 18(c), and it can be noticed that the maximum value of PCE is 76% at an input RF power of 14.9 dBm with a corresponding output voltage of 3.8 V. The graph plotted in Fig. 18(d) shows about a 100 fold logarithmic increase in the output current after combining the 21 rectifier circuits, clearly illustrating the concept of DC combining from wide scanned directions. Each identical rectifier with equal input power under linear assumption simplifies the study and gives an estimation of the overall efficiency and the enhancement of the current with the same fixed output voltage like a single rectifier unit. The class F inverse topology of the Individual rectenna elements makes sure that maximum possible PCE can be extracted. For certain directions, if there is no RF power density, the load has to be readjusted with the number of active ports for maintaining the maximum efficiency.

The DC combining efficiency is defined as the ratio of output voltage, when all the ports are simultaneously excited to the sum of the output voltages obtained from the individual rectifier units when excited independently. In the case of uniform received powers at each of the rectifier input ports, this DC combining efficiency is 100%. In the case of dynamic input powers at the individual ports, the process mentioned in [27] is followed to study the impact on efficiency. The power is varied from 15 dBm to 10 dBm from the central port to extreme ports on each side in steps of 0.5 dBm. The DC combining efficiency in this case falls to the value of 84.43%, clearly showing the impact of non-linearity of the diode.

It is possible to fabricate the complete lens structure using low cost commercially available 3D printing technology. The dimensions of the unit cells for the proposed design are selected in such a way that they are well within the least possible resolution specified by the existing 3D printing technologies. To fabricate the metallic portion covering the top and bottom portion of the lens, including the flares and the waveguide transitions, the CNC milling technology can be employed. The basic schematic of the measurement setup for the designed lens structure inside an anechoic chamber is shown in Fig. 19. The structure is placed on a rotating platform separated from the transmitting horn antenna at a distance of $'L'$ meters. The horn is fed using an RF signal source. It's power can be controlled through the amplifier and the attenuator. The output ports of the rectenna are connected to the voltmeter to measure the overall output voltage obtained from the measurement, from which the measured PCE can be calculated to further validate the simulated results. Please note that the basic setup is shown only with the single transmitting antenna. Multiple of such should be placed in order to have the predicted input RF power at each of the rectenna ports to test and validate the overall efficiency. The spectrum analyser (not shown here) can be used for measuring the power level.

## V. Conclusion

A dielectric metasurface-inspired high gain multi-beam directional Luneburg lens is designed as a wireless power transfer medium in the 5G mm wave range in this research. The lens is made up of dielectric-based glide symmetric unit cells. It is linked to a series of microwave detector-integrated multi-port tapered rectangular feeds, which convert RF energy from various directions to DC power across a combined load. The proposed structure could be a good candidate for harvesting ambient energy with a wide coverage area of 160 degrees and a power conversion efficiency of around 76% at 24 GHz with an input power of 14.9 dBm.

## Acknowledgment

The authors would like to thank Dr. Oscar Quevedo-Teruel and his group of KTH Royal Institute, Sweden for the technical inputs and valuable discussions. The authors also acknowledge the High Performance Computation facility provided by IIST, Thiruvananthapuram for carrying out the simulations.

## References

[1] O. B. Akan, O. Cetinkaya, C. Koca, and M. Ozger, "Internet of hybrid energy harvesting things," *IEEE Internet Things J.*, vol. 5, no. 2, pp. 736–746, Apr. 2018.

[2] X. Yue *et al.*, "Development of an indoor photovoltaic energy harvesting module for autonomous sensors in building air quality applications," *IEEE Internet Things J.*, vol. 4, no. 6, pp. 2092–2103, Dec. 2017.

[3] P.-H. Chen, T.-Y. Su, and P. M.-Y. Fan, "Thermoelectric energy harvesting interface circuit with capacitive bootstrapping technique for energy-efficient IoT devices," *IEEE Internet Things J.*, vol. 5, no. 5, pp. 4058–4065, Oct. 2018.

[4] F. Deng, X. Yue, X. Fan, S. Guan, Y. Xu, and J. Chen, "Multisource energy harvesting system for a wireless sensor network node in the field environment," *IEEE Internet Things J.*, vol. 6, no. 1, pp. 918–927, Feb. 2019.

[5] K. Wu, D. Choudhury, and H. Matsumoto, "Wireless power transmission, technology, and applications," *Proc. IEEE*, vol. 101, no. 6, pp. 1271–1275, Jun. 2013.

[6] K. Niotaki, S. Kim, S. Jeong, A. Collado, A. Georgiadis, and M. M. Tentzeris, "A compact dual-band rectenna using slot-loaded dual band folded dipole antenna," *IEEE Antennas Wireless Propag. Lett.*, vol. 12, pp. 1634–1637, 2013.

[7] K. Niotaki, A. Georgiadis, A. Collado, and J. S. Vardakas, "Dual-band resistance compression networks for improved rectifier performance," *IEEE Trans. Microw. Theory Techn.*, vol. 62, no. 12, pp. 3512–3521, Dec. 2014.

[8] S. Shen, C.-Y. Chiu, and R. D. Murch, "A dual-port triple-band L-probe microstrip patch rectenna for ambient RF energy harvesting," *IEEE Antennas Wireless Propag. Lett.*, vol. 16, pp. 3071–3074, 2017.

[9] S. Chandravanshi, S. S. Sarma, and M. J. Akhtar, "Design of triple band differential rectenna for RF energy harvesting," *IEEE Trans. Antennas Propag.*, vol. 66, no. 6, pp. 2716–2726, Jun. 2018.

[10] V. Kuhn, C. Lahuec, F. Seguin, and C. Person, "A multi-band stacked RF energy harvester with RF-to-DC efficiency up to 84%," *IEEE Trans. Microw. Theory Techn.*, vol. 63, no. 5, pp. 1768–1778, May 2015.

[11] C. Song *et al.*, "A novel six-band dual CP rectenna using improved impedance matching technique for ambient RF energy harvesting," *IEEE Trans. Antennas Propag.*, vol. 64, no. 7, pp. 3160–3171, Jul. 2016.

[12] S. Shen, C.-Y. Chiu, and R. D. Murch, "A broadband L-probe microstrip patch rectenna for ambient RF energy harvesting," in *Proc. IEEE Int. Symp. Antennas Propag. USNC/URSI Nat. Radio Sci. Meeting*, 2017, pp. 2037–2038.

[13] M. Arrawatia, M. S. Baghini, and G. Kumar, "Broadband bent triangular omnidirectional antenna for RF energy harvesting," *IEEE Antennas Wireless Propag. Lett.*, vol. 15, pp. 36–39, 2015.

[14] J.-H. Chou, D.-B. Lin, K.-L. Weng, and H.-J. Li, "All polarization receiving rectenna with harmonic rejection property for wireless power transmission," *IEEE Trans. Antennas Propag.*, vol. 62, no. 10, pp. 5242–5249, Oct. 2014.

[15] S. Shen, Y. Zhang, C.-Y. Chiu, and R. Murch, "An ambient RF energy harvesting system where the number of antenna ports is dependent on frequency," *IEEE Trans. Microw. Theory Techn.*, vol. 67, no. 9, pp. 3821–3832, Sep. 2019.

[16] E. Vandelle *et al.*, "Harvesting ambient RF energy efficiently with optimal angular coverage," *IEEE Trans. Antennas Propag.*, vol. 67, no. 3, pp. 1862–1873, Mar. 2019.

[17] Y.-Y. Hu, S. Sun, H. Xu, and H. Sun, "Grid-array rectenna with wide angle coverage for effectively harvesting RF energy of low power density," *IEEE Trans. Microw. Theory Techn.*, vol. 67, no. 1, pp. 402–413, Jan. 2019.

[18] U. Gustavsson *et al.*, "Implementation challenges and opportunities in beyond-5G and 6G communication," *IEEE J. Microw.*, vol. 1, no. 1, pp. 86–100, Jan. 2021.

[19] S. Ladan, S. Hemour, and K. Wu, "Towards millimeter-wave high-efficiency rectification for wireless energy harvesting," in *Proc. IEEE Int. Wireless Symp.*, 2013, pp. 1–4.

[20] N. Shinohara, K. Nishikawa, T. Seki, and K. Hiraga, "Development of 24 GHz rectennas for fixed wireless access," in *Proc. 30th URSI Gen. Assem. Sci. Symp.*, 2011, pp. 1–4.

[21] A. Collado and A. Georgiadis, "24 GHz substrate integrated waveguide (SIW) rectenna for energy harvesting and wireless power transmission," in *Proc. IEEE MTT-S Int. Microw. Symp. Dig.*, 2013, pp. 1–3.

[22] K. Hatano, N. Shinohara, T. Seki, and M. Kawashima, "Development of MMIC rectenna at 24GHz," in *Proc. IEEE Radio Wireless Symp.*, 2013, pp. 199–201.

[23] S. Ladan, A. B. Guntupalli, and K. Wu, "A high-efficiency 24 GHz rectenna development towards millimeter-wave energy harvesting and wireless power transmission," *IEEE Trans. Circuits Syst. I., Reg. Papers*, vol. 61, no. 12, pp. 3358–3366, Dec. 2014.

[24] H.-K. Chiou and I.-S. Chen, "High-efficiency dual-band on-chip rectenna for 35-and 94-GHz wireless power transmission in 0.13-$\mu$m CMOS technology," *IEEE Trans. Microw. Theory Techn.*, vol. 58, no. 12, pp. 3598–3606, Dec. 2010.

[25] B. Li, X. Shao, N. Shahshahan, N. Goldsman, T. Salter, and G. M. Metze, "An antenna co-design dual band RF energy harvester," *IEEE Trans. Circuits Syst. I., Regular Papers*, vol. 60, no. 12, pp. 3256–3266, Dec. 2013.

[26] S. Shen, Y. Zhang, C.-Y. Chiu, and R. Murch, "Directional multiport ambient RF energy-harvesting system for the Internet of Things," *IEEE Internet Things J.*, vol. 8, no. 7, pp. 5850–5865, Apr. 2021.

[27] C. Song, P. Lu, and S. Shen, "Highly efficient omnidirectional integrated multiband wireless energy harvesters for compact sensor nodes of Internet-of-Things," *IEEE Trans. Ind. Electron.*, vol. 68, no. 9, pp. 8128–8140, Sep. 2021.

[28] A. Eid, J. G. Hester, and M. M. Tentzeris, "5G as a wireless power grid," *Sci. Rep.*, vol. 11, no. 1, pp. 1–9, 2021.

[29] S. Tol, F. Degertekin, and A. Erturk, "Phononic crystal Luneburg lens for omnidirectional elastic wave focusing and energy harvesting," *Appl. Phys. Lett.*, vol. 111, no. 1, 2017, Art. no. 013503.

[30] S. H. Badri and M. Gilarlue, "Ultrashort waveguide tapers based on Luneburg lens," *J. Opt.*, vol. 21, no. 12, 2019, Art. no. 125802.

[31] J. Hunt *et al.*, "Planar, flattened Luneburg lens at infrared wavelengths," *Opt. Exp.*, vol. 20, no. 2, pp. 1706–1713, Jan. 2012.

[32] J. Hunt *et al.*, "Broadband wide angle lens implemented with dielectric metamaterials," *Sensors*, vol. 11, no. 8, pp. 7982–7991, 2011.

[33] Z. Sun *et al.*, "Discretization of two-dimensional Luneburg lens based on the correctional effective medium theory," *Opt. Exp.*, vol. 29, no. 21, pp. 33434–33444, Oct. 2021. [Online]. Available: http://www.osapublishing.org/oe/abstract.cfm?URI=oe-29-21-33434

[34] D. Headland, W. Withayachumnankul, R. Yamada, M. Fujita, and T. Nagatsuma, "Terahertz multi-beam antenna using photonic crystal waveguide and Luneburg lens," *APL Photon.*, vol. 3, no. 12, 2018, Art. no. 126105.

[35] J. Li *et al.*, "Design of a broadband metasurface Luneburg lens for full-angle operation," *IEEE Trans. Antennas Propag.*, vol. 67, no. 4, pp. 2442–2451, Apr. 2019.

[36] C. Mateo-Segura, A. Dyke, H. Dyke, S. Haq, and Y. Hao, "Flat Luneburg lens via transformation optics for directive antenna applications," *IEEE Trans. Antennas Propag.*, vol. 62, no. 4, pp. 1945–1953, Apr. 2014.

[37] A. Di Falco, S. C. Kehr, and U. Leonhardt, "Luneburg lens in silicon photonics," *Opt. Exp.*, vol. 19, no. 6, pp. 5156–5162, 2011.

[38] J. Dockrey, M. J. Lockyear, S. Berry, S. Horsley, J. R. Sambles, and A. P. Hibbins, "Thin metamaterial Luneburg lens for surface waves," *Phys. Rev. B*, vol. 87, no. 12, 2013, Art. no. 125137.

[39] R. K. Luneburg, *Mathematical Theory of Optics*. Berkeley, CA, USA: Univ. California Press, 1964.

[40] F. Ghasemifard, M. Norgren, and O. Quevedo-Teruel, "Twist and polar glide symmetries: An additional degree of freedom to control the propagation characteristics of periodic structures," *Sci. Rep.*, vol. 8, no. 1, pp. 1–7, 2018.

[41] J.-M. Poyanco, O. Zetterstrom, P. Castillo-Tapia, N. J. Fonseca, F. Pizarro, and O. Quevedo-Teruel, "Two-dimensional glide-symmetric dielectric structures for planar graded-index lens antennas," *IEEE Antennas Wireless Propag. Lett.*, vol. 20, no. 11, pp. 2171–2175, Nov. 2021.

[42] S. S. Vinnakota, R. Kumari, H. Meena, and B. Majumder, "Rectifier integrated multibeam Luneburg lens employing artificial dielectric as a wireless power transfer medium at mm wave band," *IEEE Photon. J.*, vol. 13, no. 3, pp. 1–14, Jun. 2021, Art. no. 5500314.

[43] F. Zhao, D. Inserra, G. Wen, J. Li, and Y. Huang, "A high-efficiency inverse class-F microwave rectifier for wireless power transmission," *IEEE Microw. Wireless Compon. Lett.*, vol. 29, no. 11, pp. 725–728, Nov. 2019.

[44] W.-Y. He and C. T. Chan, "The emergence of dirac points in photonic crystals with mirror symmetry," *Sci. Rep.*, vol. 5, no. 1, Feb. 2015, Art. no. 8186. [Online]. Available: https://doi.org/10.1038/srep08186

[45] M. Bozzi, S. Germani, L. Minelli, L. Perregrini, and P. de Maagt, "Efficient calculation of the dispersion diagram of planar electromagnetic band-gap structures by the MoM/BI-RME method," *IEEE Trans. Antennas Propag.*, vol. 53, no. 1, pp. 29–35, Jan. 2005.

[46] A. Coves, S. Marini, B. Gimeno, and V. Boria, "Full-wave analysis of periodic dielectric frequency-selective surfaces under plane wave excitation," *IEEE Trans. Antennas Propag.*, vol. 60, no. 6, pp. 2760–2769, Jun. 2012.

[47] D. R. Smith, S. Schultz, P. Markoš, and C. M. Soukoulis, "Determination of effective permittivity and permeability of metamaterials from reflection and transmission coefficients," *Phys. Rev. B*, vol. 65, no. 19, Apr. 2002, Art. no. 195104.

[48] Q. Chen, F. Mesa, X. Yin, and O. Quevedo-Teruel, "Accurate characterization and design guidelines of glide-symmetric holey EBG," *IEEE Trans. Microw. Theory Techn.*, vol. 68, no. 12, pp. 4984–4994, Dec. 2020.

[49] F. Giusti, Q. Chen, F. Mesa, M. Albani, and O. Quevedo-Teruel, "Efficient bloch analysis of general periodic structures with a linearized multimodal transfer-matrix approach," *IEEE Trans. Antennas Propag.*, to be published, doi: 10.1109/TAP.2022.3145485.

[50] M. Bagheriasl, O. Quevedo-Teruel, and G. Valerio, "Bloch analysis of artificial lines and surfaces exhibiting glide symmetry," *IEEE Trans. Microw. Theory Techn.*, vol. 67, no. 7, pp. 2618–2628, Jul. 2019.

[51] Q. Chen, Z. Liu, Y. Cui, H. Cai, and X. Chen, "A metallic waveguide-integrated 35-GHz rectenna with high conversion efficiency," *IEEE Microw. Wireless Compon. Lett.*, vol. 30, no. 8, pp. 821–824, Aug. 2020.

[52] C. Wang, J. Wu, and Y.-X. Guo, "A 3-D-printed wideband circularly polarized parallel-plate Luneburg lens antenna," *IEEE Trans. Antennas Propag.*, vol. 68, no. 6, pp. 4944–4949, Jun. 2020.

[53] R. M. Moreno, J. Ala-Laurinaho, and V. Viikari, "Plastic-filled dual-polarized lens antenna for beam-switching in the *ka*-band," *IEEE Antennas Wireless Propag. Lett.*, vol. 18, no. 12, pp. 2458–2462, Dec. 2019.

[54] C. Hua, X. Wu, N. Yang, and W. Wu, "Air-filled parallel-plate cylindrical modified Luneberg lens antenna for multiple-beam scanning at millimeter-wave frequencies," *IEEE Trans. Microw. Theory Techn.*, vol. 61, no. 1, pp. 436–443, Jan. 2013.

[55] X. Wang, Y. Cheng, and Y. Dong, "A wideband PCB-stacked air-filled Luneburg lens antenna for 5G millimeter-wave applications," *IEEE Antennas Wireless Propag. Lett.*, vol. 20, no. 3, pp. 327–331, Mar. 2021.

[56] H. Lu, Z. Liu, J. Liu, G. Wu, Y. Liu, and X. Lv, "Fully metallic anisotropic lens crossover-in-antenna based on parallel plate waveguide loaded with uniform posts," *IEEE Trans. Antennas Propag.*, vol. 68, no. 7, pp. 5061–5070, Jul. 2020.

[57] A. B. Numan, J.-F. Frigon, and J.-J. Laurin, "Printed $W$-band multibeam antenna with Luneburg lens-based beamforming network," *IEEE Trans. Antennas Propag.*, vol. 66, no. 10, pp. 5614–5619, Oct. 2018.

[58] S. Hemour and K. Wu, "Radio-frequency rectifier for electromagnetic energy harvesting: Development path and future outlook," *Proc. IEEE*, vol. 102, no. 11, pp. 1667–1691, Nov. 2014.

[59] J. Guo, H. Zhang, and X. Zhu, "Theoretical analysis of RF-DC conversion efficiency for class-F rectifiers," *IEEE Trans. Microw. Theory Techn.*, vol. 62, no. 4, pp. 977–985, Apr. 2014.

[60] S. Abbasian and T. Johnson, "Power-efficiency characteristics of class-F and inverse class-F synchronous rectifiers," *IEEE Trans. Microw. Theory Techn.*, vol. 64, no. 12, pp. 4740–4751, Dec. 2016.

[61] Q. Chen, X. Chen, H. Cai, and F. Chen, "A waveguide-fed 35-GHz rectifier with high conversion efficiency," *IEEE Microw. Wireless Compon. Lett.*, vol. 30, no. 3, pp. 296–299, Mar. 2020.

[62] Q. Chen, X. Chen, H. Cai, and F. Chen, "Schottky diode large-signal equivalent-circuit parameters extraction for high-efficiency microwave rectifying circuit design," *IEEE Trans. Circuits Syst., II, Exp. Briefs*, vol. 67, no. 11, pp. 2722–2726, Nov. 2020.

[63] A. N. Parks and J. R. Smith, "Sifting through the airwaves: Efficient and scalable multiband RF harvesting," in *Proc. IEEE Int. Conf. RFID*, 2014, pp. 74–81.

[64] Y.-J. Ren and K. Chang, "5.8-GHz circularly polarized dual-diode rectenna and rectenna array for microwave power transmission," *IEEE Trans. Microw. Theory Techn.*, vol. 54, no. 4, pp. 1495–1502, Jun. 2006.